

Monitoring Geological Storage of CO₂ – A New Rock Physics Model to Estimate Saturation

Manzar Fawad (✉ manzar.fawad@geo.uio.no)

University of Oslo

Nazmul Haque Mondol

University of Oslo

Research Article

Keywords: geological storage, CO₂, rock, physics model, estimate, saturation, global warming crisis, injection, hydrocarbon

Posted Date: October 22nd, 2021

DOI: <https://doi.org/10.21203/rs.3.rs-966923/v1>

License: © ⓘ This work is licensed under a Creative Commons Attribution 4.0 International License.

[Read Full License](#)

Monitoring geological storage of CO₂ – A new rock physics model to estimate saturation

Manzar Fawad¹ ✉, Nazmul Haque Mondol^{1,2}

¹Department of Geosciences, University of Oslo, Oslo, Norway. ²Norwegian Geotechnical Institute (NGI), Oslo, Norway. ✉e-mail: manzar.fawad@geo.uio.no

Abstract

To mitigate the global warming crisis, one of the effective ways is to capture CO₂ at an emitting source and inject it underground in saline aquifers, depleted oil and gas reservoirs, or in coal beds. This process is known as carbon capture and storage (CCS). With CCS, CO₂ is considered a waste product that has to be disposed of properly, like sewage and other pollutants. While and after CO₂ injection, monitoring of the CO₂ storage site is necessary to observe CO₂ plume movement and detect potential leakage. For CO₂ monitoring, various physical property changes are employed to delineate the plume area and migration pathways with their pros and cons. We introduce a new rock physics model to facilitate the time-lapse estimation of CO₂ saturation and possible pressure changes within a CO₂ storage reservoir based on physical properties obtained from the prestack seismic inversion. We demonstrate that the CO₂ plume delineation, saturation, and pressure changes estimation are possible using a combination of Acoustic Impedance (AI) and P- to S-wave velocity ratio (V_p/V_s) inverted from time-lapse or four-dimensional (4D) seismic. We assumed a scenario over a period of 40 years comprising an initial 25 year injection period.

Our results show that monitoring the CO₂ plume in terms of extent and saturation can be carried out using our rock physics-derived method. The suggested method without going into the elastic moduli level handles the elastic property cubes which are commonly obtained from the prestack seismic inversion. Pressure changes quantification is also possible within un-cemented sands; however, the stress/cementation coefficient in our proposed model needs further study to relate that with effective stress in various types of sandstones. The three-dimensional (3D) seismic usually covers the area from the reservoir's base to the surface makes it possible to detect the CO₂ plume's lateral and vertical migration. However, the comparatively low resolution of seismic, the inversion uncertainties, lateral mineral, and shale property variations are some limitations, which warrant consideration. This method can also be applied for the exploration and monitoring of hydrocarbon production.

Introduction

Subsurface CO₂ storage is not a new concept. For decades, the oil and gas industry has been re-injecting the CO₂ produced along with the hydrocarbon gases^{1,2}. CO₂ injection has also been used for enhanced oil recovery^{3,4}. Carbon capture and storage (CCS) has the potential to significantly reduce CO₂ build-up in the atmosphere from fossil fuel use; however, large-scale subsurface CO₂ storage still may pose different technical and social challenges⁵.

Buoyancy trapping is the key process for CO₂ storage during the injection and early stage of storage⁵. Therefore, the CO₂ is injected at the base of the reservoir, and the plume migrates laterally within the most permeable beds until it finds a vertical passage (fault or fracture) to move upwards and accumulate below the base of the caprock. The plume behavior is a function of the horizontal and vertical heterogeneities within the reservoir. The thin clay and silt layers or carbonate laminations may facilitate lateral distribution of CO₂ in the storage reservoir. For example, in the Sleipner CCS project, the four-dimensional (4D) or time-lapse seismic enables one to trace the migration path and subsequent accumulation of the CO₂ plume⁶. The other CO₂ trapping mechanisms are residual gas trapping, solubility trapping, and mineral trapping. The time-lapse or 4D seismic is carried out to

51 monitor the CO₂ plume migration within the storage reservoir (for example, in a saline aquifer), and to
52 identify a possible vertical CO₂ leakage into the shallower strata or surface.

53
54 There are several methods in use for seismic fluid prediction⁷. Many provide qualitative hydrocarbon
55 indication, whereas few techniques are quantitative. The qualitative methods comprise Amplitude-
56 Variation-with-Offset (AVO) analysis⁸⁻¹¹, AVO cross plotting^{12,13}, Lambda-Mu-Rho (LMR)¹⁴,
57 Extended Elastic Impedance (EEI)¹⁵, and Curved Pseudo Elastic Impedance (CPEI)^{16,17}. The examples
58 of quantitative methods are Acoustic Impedance versus P- to S-wave velocity ratio (AI-versus-Vp/Vs)
59 rock physics template¹⁸⁻²⁰, Multi-Attribute Rotation Scheme (MARS)²¹, Inverse Rock Physics
60 Modelling (IRPM)^{22,23}, and technique to discriminate saturation and pressure from 4D seismic using
61 near and far offset stacks²⁴.

62
63 A practical approach suggested for fluid saturation discrimination²⁵ using seismic data employed a
64 method similar to LMR¹⁴. Lamé parameters were calculated, however the fluid saturation was
65 suggested to be estimated on a ρ/μ versus λ/μ plane as opposed to the LMR method where a $\lambda\rho$ versus
66 $\mu\rho$ was used to differentiate various facies (ρ is bulk density, λ is incompressibility, and μ is shear
67 modulus). Two-dimensional permeability modelling²⁶ of CO₂ saturation, distribution and seismic
68 response showed CO₂ trapping, and the P-wave velocity (Vp) and water saturation (Sw) relationship
69 were mostly function of the Dykstra-Parson²⁷ coefficients. Executing a workflow for forward
70 modeling²⁸ of time-lapse seismic data indicated that a high signal-to-noise ratio was needed to detect
71 the CO₂ leakage at the model site. Both^{26,28} the studies used Gassmann equations²⁹ for fluid
72 substitution. Another three-dimensional (3D) modelling study³⁰ related AI changes with the water
73 saturation (Sw), and quantitatively demonstrated that seismic amplitudes can be more precise than
74 seismic impedances for quantifying Sw changes with 4D seismic data.

75
76 A seismic profile can be defined as an array of processed seismic traces. Each trace represents the
77 convolution of a source wavelet with an input reflectivity sequence where each reflectivity spike
78 depicts the contrast in acoustic impedance (AI = P-wave velocity × Bulk Density) across a geological
79 interface. A seismic inversion is carried out to convert the interface property (reflectivity) to a physical
80 rock property such as AI^{31,32}. With the advent of AVO/prestack inversion, it became possible to obtain
81 the Shear wave (Vs) information also, usually in the form of shear impedance (SI) from the AVO far-
82 offset data. Various forms of Fatti's equation³³ are used for AVO inversion; one of that is³⁴:

$$84 \quad R_P(\theta) \approx (1 + \tan^2\theta) \frac{\Delta AI}{2AI} - 8 \left(\frac{V_S}{V_P}\right)^2 \sin^2\theta \frac{\Delta SI}{2SI} \quad (1)$$

85
86 where $R_P(\theta)$ is the P-wave reflectivity at an angle θ , this angle is the average of incidence and
87 transmission angles, Vp is P-wave velocity, Vs is S-wave velocity, $\Delta AI/AI$ and $\Delta SI/SI$ are acoustic
88 impedance and shear impedance reflectivities, respectively.

89
90 Rock physics models represent the link between the reservoir properties (e.g., porosity, clay content,
91 sorting, lithology, saturation) and seismic-derived elastic properties (e.g., AI, SI or Vp/Vs ratio). One
92 of the existing models comprised a hybrid modeling approach¹⁹ using the AI versus Vp/Vs RPT
93 applied specifically to sandstones employing a physical-contact theory, i.e., the Hertz-Mindlin model³⁵
94 combined with theoretical elastic bounds, e.g., the Hashin-Shtrikman bounds³⁶ simulating the porosity
95 reduction trend associated with depositional sorting and diagenesis. For soft shales, the seismic
96 properties were estimated as a function of pore shape. Gassmann fluid substitution²⁹ was carried out to
97 estimate the effect of varying gas versus water saturation in the sand layers, whereas Backus average³⁷
98 was used to predict the effective seismic properties for changing net-to-gross (N/G ratios)¹⁹. However,
99 it has been demonstrated²² that even with the standard rock physics template (RPT) of AI versus
100 Vp/Vs¹⁸⁻²⁰, it is difficult to know whether the model is adequately calibrated to the data or how it can
101 be interpreted. Furthermore, there are nonunique solutions resulting in various combinations of

102 porosity, lithology, and fluid saturations that have the same Vp/Vs ratio and AI, using the same rock
 103 physics model²².

104

105 In this study we introduce a new interactive rock physics model that directly relates AI with the Vp/Vs
 106 ratio for predicting fluid saturation (S_{fl}). The model can be calibrated with the well-log data
 107 interactively, without using the Hertz-Mindlin model³⁵, Hashin-Shtrikman bounds³⁶, or Gassmann
 108 fluid substitution²⁹. The suggested model is non-linear similar to CPEI^{16,17}, but with physical meanings
 109 and flexibility that can readily be applied to the seismic-derived AI and Vp/Vs cubes to estimate S_{fl} .
 110 We came up with a similar equation in a previous publication³⁸ to calculate shale volume (Vsh) based
 111 on the AI, Vp/Vs ratio domain.

112

113 Following is the proposed model to estimate the target fluid saturation (S_{fl}) in fraction using the AI
 114 and Vp/Vs ratio data obtained by AVO inversion:

115

$$116 \quad S_{fl} = \frac{\left\{ \rho_{ma} + \left[1 - \left(\frac{V_S}{V_P G \alpha} \right)^{\frac{1}{n}} \right] (\rho_w - \rho_{ma}) - AI \left[\frac{1}{V_{Pma}} + \left(1 - \left(\frac{V_S}{V_P G \alpha} \right)^{\frac{1}{n}} \right) \left(\frac{1}{V_{Pw}} - \frac{1}{V_{Pma}} \right) \right] \right\}}{\left\{ \left[1 - \left(\frac{V_S}{V_P G \alpha} \right)^{\frac{1}{n}} \right] \left[AI \left(\frac{1}{V_{Pfl}} - \frac{1}{V_{Pw}} \right) - (\rho_{fl} - \rho_w) \right] \right\}} \quad (2)$$

117

118 where V_{Pma} and V_{Pw} are the P-wave velocities of the mineral matrix, and brine respectively, V_{Pfl} is the
 119 apparent P-wave velocity of the target fluid, ρ_{ma} is the density of mineral grains, ρ_{fl} is the apparent
 120 density of the target fluid, ρ_w is the density of brine, AI is acoustic impedance, G is the
 121 mineralogy/shaliness coefficient, α is Vs/Vp ratio of the mineral/rock matrix, and n is the
 122 stress/cementation coefficient. The water saturation (S_w) can be calculated subsequently ($S_w = 1 - S_{fl}$).

123

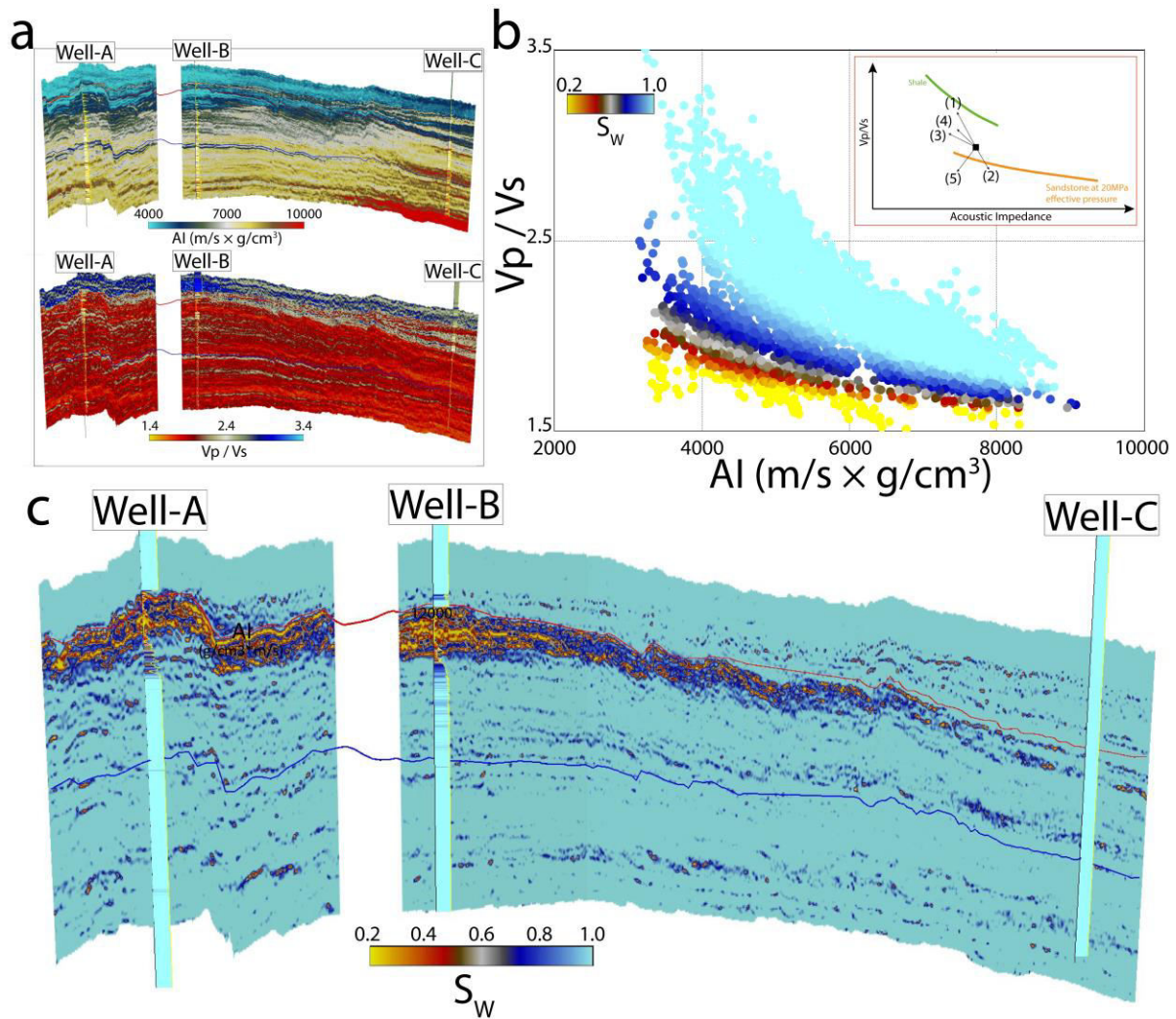
124 As mentioned previously, the AI and Vp/Vs ratio are obtained by inverting seismic data (Fig. 1a). AI
 125 increases and Vp/Vs ratio decreases typically with increasing burial depth due to a decrease in
 126 porosity. If a low-density fluid (hydrocarbon or CO₂) replaces the in-situ brine, a reduction both in AI
 127 and Vp/Vs values is expected depending upon the substituted fluid's density. We came up with Eq. 2
 128 that relates AI with Vp/Vs ratio to isolate the target fluid saturation from the brine saturated sandstone
 129 compaction trend on the AI versus Vp/Vs ratio plane (Figs. 1b&c). One can calibrate the model using
 130 nearby well data (Well-A in this case, see Methods section).

131

132 This technique will help to monitor a CO₂ plume in the subsurface for lateral and vertical migration.
 133 The proposed method will be useful for reliable control on the CO₂ injection and sequestration
 134 processes. Other uses could be oil and gas production monitoring and hydrocarbon exploration.

135

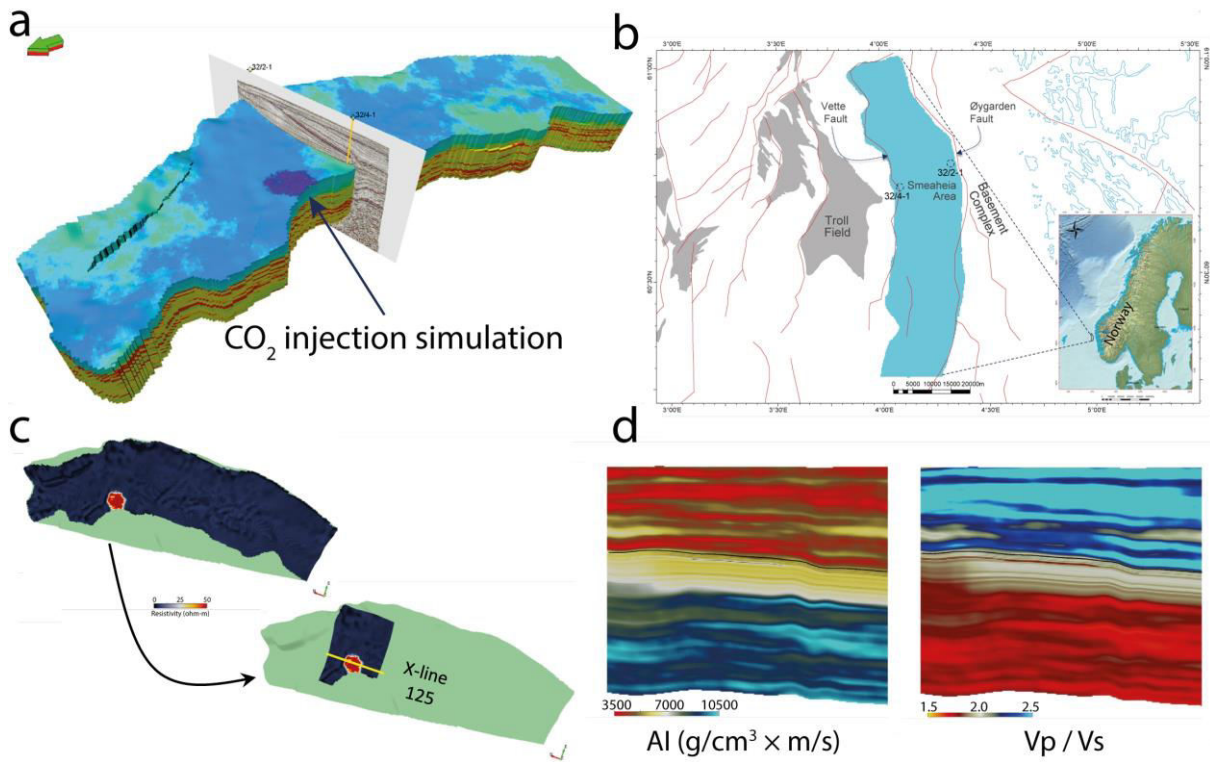
136



137
 138 Figure 1. An example of a fluid response in a hydrocarbon field on the Norwegian Continental Shelf,
 139 a) AI and Vp/Vs ratio profiles obtained from a seismic inversion with hydrocarbon-bearing wells
 140 (Well-A, Well-B), and a dry well (Well-C), b) Data along the seismic lines plotted on the AI-Vp/Vs
 141 plane show that the fluid effect can be isolated and quantified using our proposed rock physics model,
 142 c) the resulting fluid saturation profile indicating the hydrocarbon anomaly and its extent. The inset in
 143 (b) does also show how the brine saturated sandstone will plot as the (1) shale content increase, (2)
 144 the amount of cement increase, (3) the porosity in the sandstone increase, (4) the effective stress in the
 145 formation decrease and (5) the saturation of gas increase within the sandstone¹⁸.

146
 147 Similar to our previous study³⁹, we used the synthetic elastic property data from the Norwegian
 148 Geotechnical Institute (NGI). NGI generated Vp, Bulk Density, and Resistivity⁴⁰ properties using grids
 149 from a reservoir model by the Northern Light project⁴¹ (Fig. 2a). Additionally, we calculated the Vs
 150 data to generate the Vp/Vs ratio cubes (see details in “Methods” section). The reservoir model was a
 151 simulation of one of the potential CO₂ storage sites in the northern North Sea called Smeaheia (Fig.
 152 2b). The Smeaheia area is bounded by a fault array separating the Troll oil and gas field in the west
 153 and the Basement Complex in the east³⁸. The primary CO₂ storage reservoir in the Smeaheia area is
 154 Sognefjord Formation (Upper Jurassic) sandstone, capped by the Draupne and Heather Formation
 155 (Upper Jurassic) shales^{38,42} (Fig. 3). The amount of CO₂ to be stored was 1.3 Mt/year employing an
 156 injection period of 25 years with an injection rate of 200 tons/hr. We sliced out the AI and Vp/Vs ratio
 157 cubes covering only the injection and storage area to reduce computation time and converted the cubes
 158 to a depth-domain seismic format with inline and crossline profiles (Fig. 2c). We assumed that the AI
 159 and the Vp/Vs cubes were the actual values obtained from the seismic inversion (Fig. 2d).

160



161
162

163 Figure 2. a) The original Northern Light project⁴¹ simulation modelling grid, b) location of the
164 modelled grid area (light blue) in the northern North Sea, maps modified from the Norwegian
165 Petroleum Directorate (NPD) data⁴³, c) example of a property grid carved out to a seismic formatted
166 cube covering only the injection and storage area, d) AI and Vp/Vs ratio profiles along crossline 125
167 shown in (c), the example here is of the year 2050, the effect of injected CO₂ on both AI and Vp/Vs
168 ratio is very subtle (Figure modified after ³⁹).

169

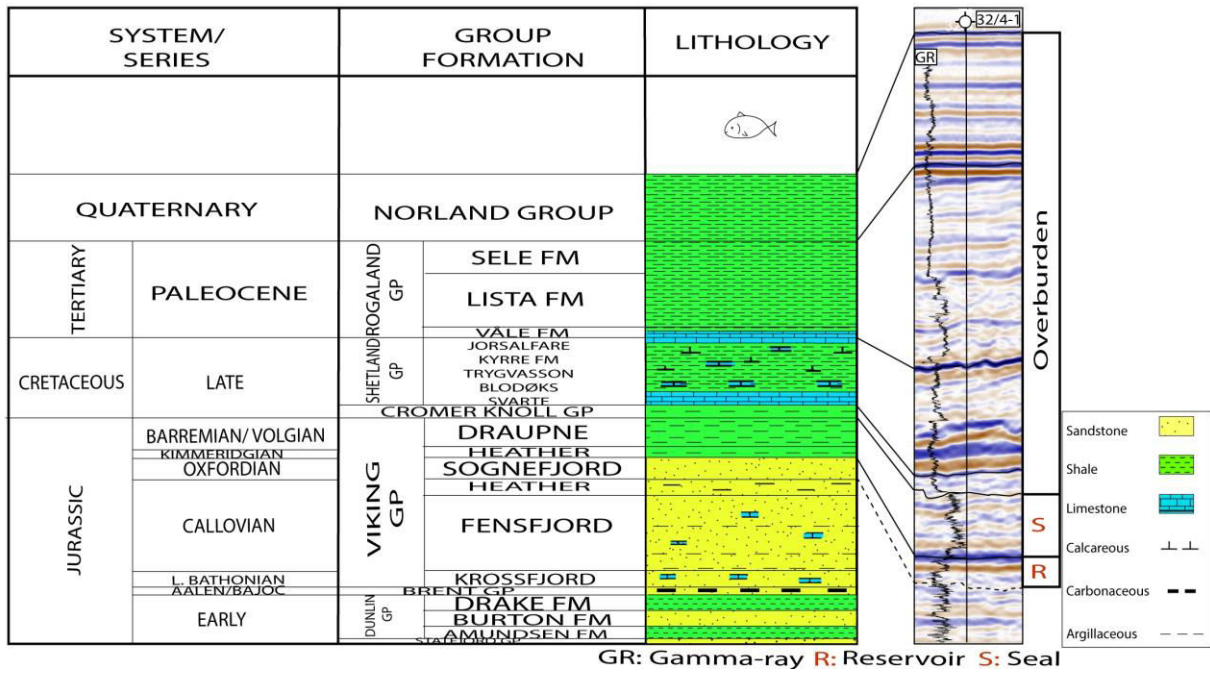
170 We assumed a monitoring scenario over 40 years, with injection starting in 2020 for 25 years, keeping
171 an assumption that the time-lapsed seismic surveys were acquired every 10 years. This study also has
172 implications for hydrocarbon exploration and monitoring of oil and gas production. The anisotropy in
173 physical properties, CO₂ dissolution, and chemical reaction with rock grains and their effect on the AI
174 and Vp/Vs ratio are not taken into account.

175

176

177

178



179
180

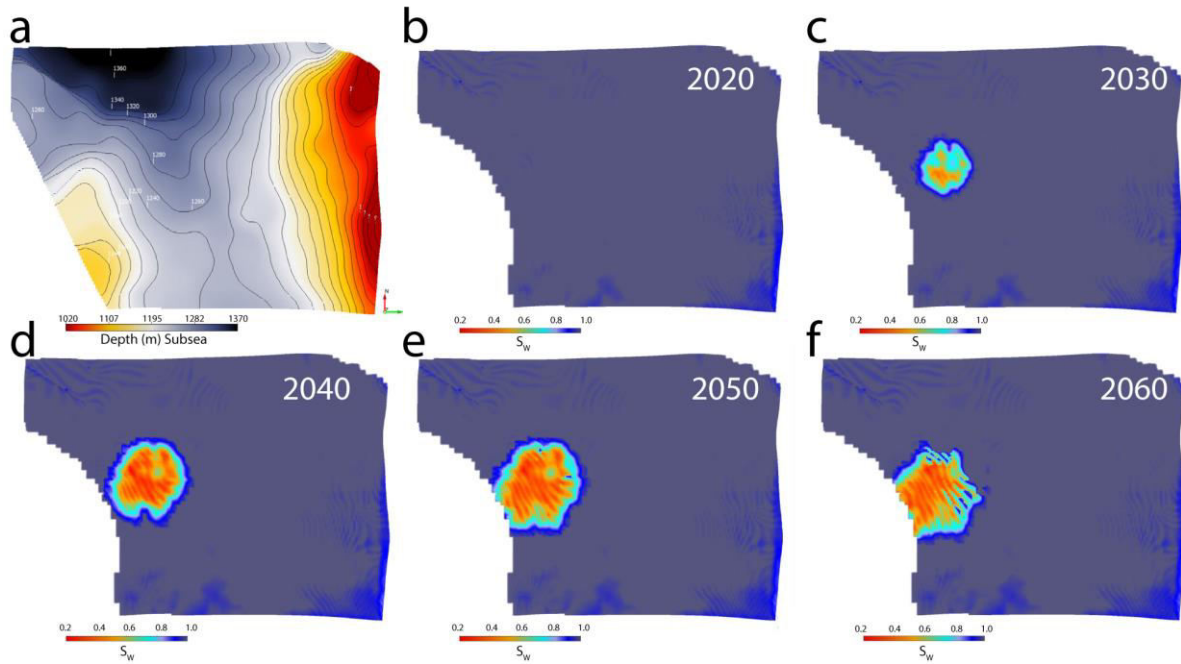
181 Figure 3. A generalized Jurassic to Quaternary stratigraphic succession in the study area (modified
182 from^{38,44}). The base Sognefjord Fm contact with Heather Fm is not so obvious on seismic, therefore, it
183 is shown as dotted line.

184

185 **Results and Discussion**

186

187 We demonstrate a scenario where we have time-lapsed/4D seismic data from 2020 before injection to
188 the year 2060. The top of the Sognefjord Formation reservoir lies between 1020m and 1370m below
189 mean sea level (Fig. 4a). The reservoir is brine saturated before CO₂ injection in 2020 (Fig. 4b). Both
190 the reservoir AI and Vp/Vs ratio supposedly obtained from prestack inversion decreases where the
191 CO₂ plume replaces the in-situ brine. Therefore, the estimated saturations from AI and Vp/Vs ratio
192 very well define the plume boundaries and reservoir inhomogeneity (Figs. 4c-f). We can also see the
193 plume boundary systematically increasing with the passage of years and moving towards the
194 southwest in the up-dip direction. The injection stopped in 2045, therefore a water breach within the
195 plume along the northeastern boundary is apparent as the plume migrates southwestwards in the panel
196 showing the year 2060 (Fig. 4f).



197
198

199 Figure 4. The top Sognefjord Formation reservoir depth surface (a) draped on saturation cubes in years
200 b) 2020, c) 2030, d) 2040, e) 2050, and f) 2060. The CO₂ plume moves up-dip over time towards the
201 southwest.

202

203 Discrimination between pressure and fluid saturation affects

204

205 On the AI versus Vp/Vs crossplot, there is a systematic decrease in water saturation within reach of
206 the CO₂ plume from 2020 to 2060 (Fig. 5). The CO₂ injection started in 2020 and was completed in
207 2045. In the panels representing the year 2050, the gas saturated points show a little scatter that
208 increases in 2060. This point scatter could be due to the diffusion and up-dip migration of gas.

209

210 With the increase in time from 2020 to 2040, there is a subtle shift in the brine-sand trend (Fig. 5a-c)
211 in the direction '4' shown in the inset of Figure 1b. We calibrated the brine-sand trend for saturation
212 calculations by changing the value of stress/cement coefficient 'n'. This change in 'n' values is a good
213 indication of reducing effective stress due to the increase in pore pressure (approximately 10 Bar/1
214 MPa). The brine-saturated sand trend stays roughly the same in the panel covering the end of injection
215 year, i.e., 2045 (Fig. 5d), and the subsequent survey in 2060 (Fig. 5e). One should bear in mind that
216 the Sognefjord Formation sandstone reservoir is predominantly un-cemented³⁸. We cannot expect a
217 similar change of brine trend with a change in effective stress within deeper quartz cemented
218 sandstones. Relating the change in 'n' values with the effective stress in various un-cemented sands
219 needs further studies.

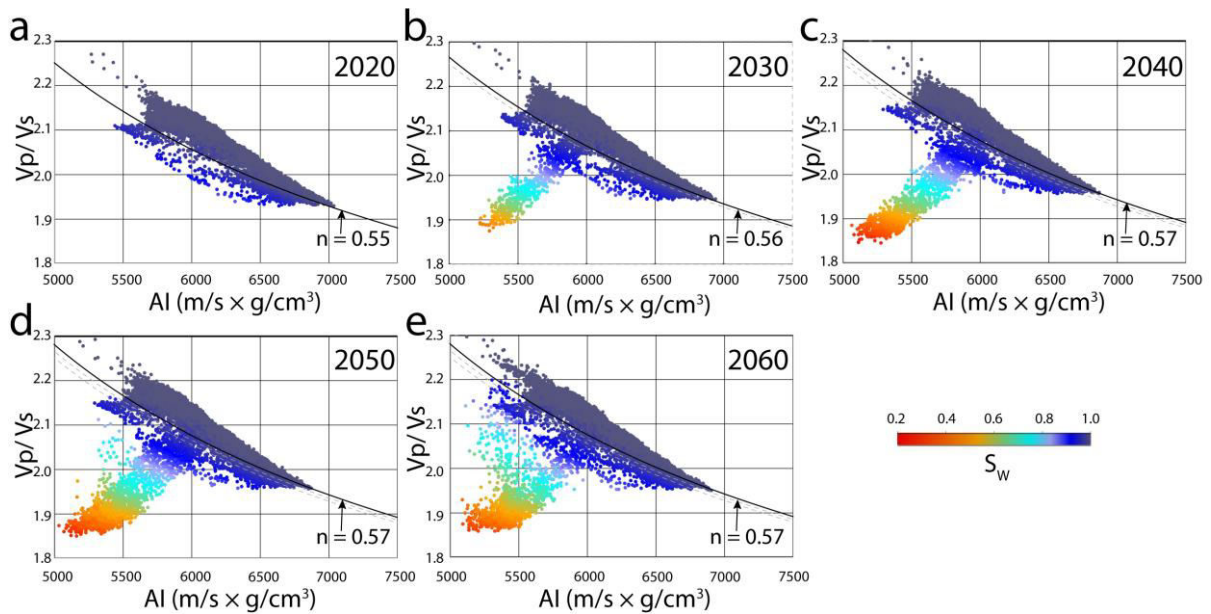
220

221 Advantages of our suggested rock physics model

222

223 In the traditional AI-Vp/Vs rock physics template^{18,19}, the dry sandstone is modeled by combining
224 Hertz-Mindlin contact theory³⁵ and Hashin-Shtrikman³⁶ interpolation, and finally Gassmann fluid
225 substitution²⁹ is performed to estimate the effect of varying fluid saturation in the sand layers. The
226 modelling typically starts from the high-porosity end member interpolated to zero porosity matrix
227 mineral point employing equations that use the rock bulk (K) and shear (μ) moduli as input. The model
228 we suggested (Eq. 2) does not require computations at the elastic moduli level. The matrix point is
229 defined on the AI versus Vp/Vs plane on the basis of coefficient α that is Vs/Vp ratio of the
230 mineral/rock matrix (Fig. 6). While keeping the matrix point at the same position, the gradient of the
231 line interpolating between the matrix point with the high-porosity end member can be changed using
232 the coefficient 'n'. This interpolation defines the brine-sand (100% Sw) line that can be adjusted to

233 calibrate with the stress or cementation condition of the target layer. Changing the shale/mineralogy
 234 coefficient ‘G’ results in a static vertical shift of the brine-sand line that helps adjusting with the N/G
 235 ratio of the target layer data. The saturation contours adjust themselves with respect to the brine-line
 236 according to the given apparent P-wave velocity and density of the target fluid (V_{Pfl} and ρ_{fl} ,
 237 respectively). This procedure does not require Gassmann substitution²⁹ as one needs in the traditional
 238 AI-Vp/Vs rock physics template. Also, the model works for both un-cemented and cemented
 239 sandstones. In the case of Extended Elastic Impedance (EEI)¹⁵, the calculated properties (for instance,
 240 S_w) appear linear on the AI-Vp/Vs ratio plane; however, the actual sandstone exhibits a nonlinear
 241 curvature¹⁶. This nonlinearity is captured by our model, same as the curved pseudo-elastic impedance
 242 (CPEI)^{16,17}; however, our suggested model is quantitative and, as discussed above, flexible in terms of
 243 grain mineralogy and fluid density. The LambdaRho-MuRho¹⁴ calculations to differentiate lithology
 244 and fluid content introduce error and bias because of squaring the impedances¹⁸. The equation we
 245 present does not contain any squared factors, thus preventing additional errors.
 246



247
 248
 249 Figure 5. Data points sampled at regular intervals on the top Sognefjord Formation sandstone surface
 250 are displayed on the AI versus V_p/V_s ratio plane color-coded by S_w for years a) 2020, b) 2030, c)
 251 2040, d) 2050, and d) 2060. The position of the brine-saturated sandstone line with corresponding 'n'
 252 values is also shown in each panel.
 253

254 For subsurface storage, CO_2 is injected in the supercritical phase to a depth where the temperature and
 255 pressure keep the gas in the same phase. This approach maximizes the use of available storage volume
 256 in the pore spaces within a reservoir. Therefore, the optimum depth for storage is from 1 to 3 km
 257 depth⁵. The quartz cementation approximately starts below 2000 m from the seafloor in the North Sea,
 258 where the temperature becomes more or less 70°C. We demonstrated that there is a possibility of
 259 quantifying the change in pressure within the un-cemented reservoir sands; therefore, using our
 260 suggested model will be helpful in that case. In both un-cemented and cemented sandstone reservoirs,
 261 if the supercritical CO_2 plume converts to gas at some point in time due to a decrease in pore pressure,
 262 the subsequent time-lapse S_w calculations using our model will yield a value less than 0 indicating a
 263 pressure drop.
 264

265 Limitations and pitfalls

266
 267 This method can be applied only in siliciclastics as the carbonates exhibit a different V_p to V_s
 268 relationship. There is a difference in resolution between the wireline log data and seismic; therefore,
 269 calibrating the model using wireline logs often yields an up-scaled profile in seismic.
 270

271 Most of the method's uncertainties are associated with the inversion procedure itself⁴⁵. First of all, the
272 inversion is nonunique, i.e., several different solutions (combinations of elastic parameters) may yield
273 the same seismic response. Moreover, the need for an initial low-frequency model poses a main
274 uncertainty during the simultaneous AVO inversion. If the low-frequency model is far away from the
275 truth, the inversion cannot predict the correct answer. Since the low-frequency model is generated
276 from the well-log data and seismic velocities, it becomes more uncertain away from the well control
277 affecting offset-to-angle calculations⁴⁵. To verify the predictions of our suggested technique in CO₂
278 storage monitoring, saturation calculations from monitoring wells with time-lapse logging can be
279 employed. In case of a hydrocarbon field, comparison with the existing wells (not used for model
280 calibration) can help examining the model-derived saturation accuracy, as in case of Well-B in Figure
281 1. Using this procedure in frontier areas to predict hydrocarbon may be complemented by our
282 proposed method that combines seismic with Controlled Source Electro-Magnetic (CSEM)³⁹.
283

284 The other uncertainties are the lateral changes in mineralogy or shale volume within the reservoir,
285 resulting in a slight change in the reference brine saturated trend compared to the original calibration.
286 To address this uncertainty, a stochastic approach can be used, taking for example, a normal
287 distribution of the input parameters. In the case of two fluids present in a reservoir, i.e., oil with a gas
288 cap are difficult to distinguish; therefore, calibration with gas parameters can be employed to represent
289 the combined influence of the two fluids. A surface draped on an Sw cube may exhibit an 'aliasing
290 pattern' (Fig. 4d-f) depending on the data sampling frequency. The stochastic solution will also resolve
291 this imaging problem.
292

293 **Conclusions**

294
295 The seismic method generally provides the subsurface structural and stratigraphic information.
296 Prestack seismic data can be inverted to provide quantitative information on physical properties such
297 as acoustic impedance (AI), shear impedance (SI), and Vp/Vs ratio. Though seismic velocities are
298 moderately sensitive to the change in saturation, using a combination of AI and Vp/Vs ratio can
299 discriminate fluids and their saturations in many situations.
300

301 We introduced a new rock physics model that calculates fluid saturations onto the AI versus Vp/Vs
302 ratio plane directly using the cubes inverted from seismic. Without going into the elastic moduli level
303 and Gassmann substitution, the model can be calibrated using well log data by comparing the S_w
304 calculated from AI and Vp/Vs curves with the Archie-derived S_w. We demonstrated using this model
305 that the elastic properties inverted from seismic help predict CO₂ saturation in a reservoir during and
306 after injection in a subsurface geological CO₂ storage.
307

308 Modeling using our proposed approach showed that CO₂ saturation estimation and the plume area
309 delineation is possible using acoustic impedance (AI) and Vp/Vs ratio. The change in pore-pressure
310 estimation is also possible by quantifying the change in brine-sand trend using the stress/cementation
311 coefficient 'n' in un-cemented sand reservoirs. The relation of 'n' with different effective stresses in
312 various uncemented sands warrants further investigation.
313

314 One can also use the suggested procedure to monitor oil and gas production and for hydrocarbon
315 exploration. The main uncertainties and pitfalls of the method come from the inherent inversion
316 problems. We expect with the improvement in prestack inversion technology, the predictability of our
317 rock physics model will increase.
318

319 **Methods**

320
321 We generated a rock physics model assuming that a reservoir consists of a rock matrix, pore spaces
322 containing salt water (brine), and other fluids (e.g., CO₂, or hydrocarbon). According to the
323 assumption, the total volume of rock comprising the matrix and the fluids in the pore spaces is equal to
324 1. Wyllie⁴⁶ approximated the relation between velocity and volumes in sedimentary rocks with the
325 following expression:

326

327

$$\frac{1}{V_P} = \frac{(1-\emptyset)}{V_{P_{ma}}} + \frac{S_{fl}\emptyset}{V_{P_{fl}}} + \frac{(1-S_{fl})\emptyset}{V_{P_w}} \quad (3)$$

328

329

330

331

332

333

334

335

336

337

338

$$\rho_b = (1 - \emptyset)\rho_{ma} + S_{fl}\emptyset\rho_{fl} + (1 - S_{fl})\emptyset\rho_w \quad (4)$$

339

340

341

342

343

$$\emptyset = \frac{\left(\rho_{ma} - \frac{AI}{V_{P_{ma}}}\right)}{\left\{AI\left[S_{fl}\left(\frac{1}{V_{P_{fl}}} - \frac{1}{V_{P_w}}\right) + \left(\frac{1}{V_{P_w}} - \frac{1}{V_{P_{ma}}}\right)\right] - [S_{fl}(\rho_{fl} - \rho_w) + (\rho_w - \rho_{ma})]\right\}} \quad (5)$$

344

345

Employing a relation between the S-wave velocity and the P-wave velocity⁴⁷:

346

$$\frac{V_P}{V_S} = \frac{1}{[G\alpha(1-\emptyset)^n]} \quad (6)$$

347

348

349

350

351

352

353

354

355

356

357

358

359

360

361

362

363

364

365

366

367

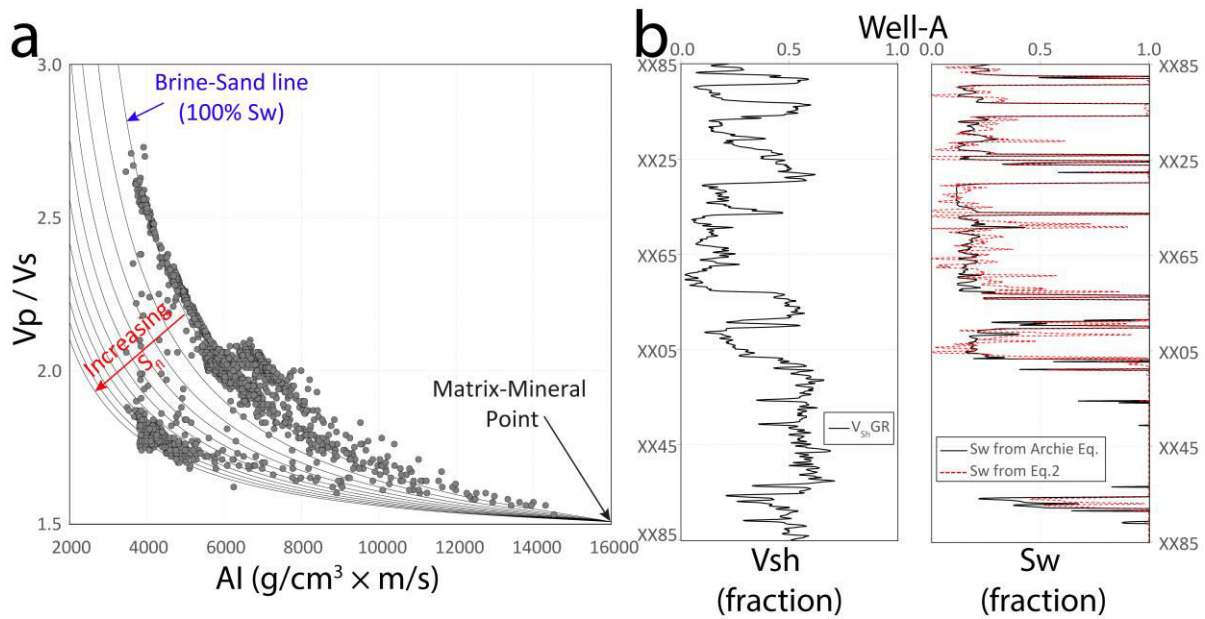
368

369

where AI is acoustic impedance. We can calculate the V_p/V_s ratio against a given AI by substituting \emptyset from Eq. 5. Changing the mineralogy/shaliness coefficient 'G' results in a vertical static shift in the curved iso-saturation lines, α is V_s/V_p ratio of the mineral/rock matrix that defines the matrix-mineral pole on the AI versus V_p/V_s ratio plane. The stress/cementation coefficient 'n' controls the slope of the iso-saturation curved lines and may be selected in a formation zone depending on the level of stress, compaction, or cementation. The relevant constants may be taken from literature⁴⁸ and vendor's logging chart books.

From this function (Eq. 6), we can define a set of lines representing different fluid saturations converging at the 100% matrix-mineral pole on the AI versus V_p/V_s ratio plane (Fig. 6a). Iterating the values of 'G' and 'n' one can calibrate the wet trend of the well data with the 100% S_w line (Fig. 6a). Finally, we find out the values of the target fluid's apparent density (ρ_{fl}) and apparent P-wave velocity ($V_{P_{fl}}$) by iterating their values until the S_w is computed using Eq. 2 calibrates with the Archie S_w ⁴⁹ (Fig. 6b). The apparent fluid velocity ($V_{P_{fl}}$) and density (ρ_{fl}) values may be fictitious as their difference from the actual values could depend on factors such as the mode of saturation (continuous⁵⁰ or patchy⁵¹) etc.

The calibrated model then can be applied by inputting the seismic-derived AI and V_p/V_s cubes to obtain an S_w cube. A similar approach with different initial assumptions leads to the derivation of a rock physics relation for estimating shale volume (V_{sh}) from inverted data³⁸.



370
371

372 Figure 6. Method of calibrating the rock physics model a) Aligning the brine-saturated sandstone
373 trend in the data with the reference 100% S_w line onto the Acoustic impedance versus V_p/V_s ratio
374 plane by iterating the 'G' and 'n' values. b) Calibrating S_w by iterating the apparent velocity and density
375 of the hydrocarbon until the S_w curve is obtained from Eq. 2 correlates with the Archie S_w ⁴⁹.
376

377

378 The original reservoir simulation model was conceived by the Northern Light project⁴¹. The model
379 simulated one of the potential CO_2 storage sites "Smeaheia" in the northern North Sea. The injection
380 rate used was 1.3 Mt/year with an injection period of 25 years (from 2020 to 2045). The post-injection
381 period was simulated for 100 years. Subsequently, using results from reservoir simulation the
382 Norwegian Geotechnical Institute (NGI) generated V_p , Bulk Density and Resistivity⁴⁰ properties. For
383 the present study, we generated V_s data additionally to obtain V_p/V_s ratio cubes by applying
384 Castagna's equation⁵² on the baseline V_p . We assumed that there was no change in shear modulus as
385 the gas injection proceeded, while the change in the density within the plume area was substituted
386 accordingly. Finally, we used the AI ($V_p \times$ Bulk Density) and V_p/V_s property cubes in the present
387 study.

388

388 References

389

390 1. Mathieson, A., Midgely, J., Wright, I., Saoula, N. & Ringrose, P. In Salah CO_2 Storage JIP: CO_2

391

sequestration monitoring and verification technologies applied at Krechba, Algeria. *Energy*

392

Procedia **4**, 3596–3603 (2011).

393

2. Buscheck, T. A., White, J. A., Carroll, S. A., Bielicki, J. M. & Aines, R. D. Managing geologic CO_2

394

storage with pre-injection brine production: a strategy evaluated with a model of CO_2 injection at

395

Snøhvit. Energy & Environmental Science **9**, 1504–1512 (2016).

396

3. Perera, M. S. A. *et al.* A review of CO_2 -enhanced oil recovery with a simulated sensitivity analysis.

397

Energies **9**, 481 (2016).

- 398 4. Ampomah, W. *et al.* Evaluation of CO₂ storage mechanisms in CO₂ enhanced oil recovery sites:
399 application to morrow sandstone reservoir. *Energy & Fuels* **30**, 8545–8555 (2016).
- 400 5. Riley, N. Geological storage of carbon dioxide. *Issues in Environmental Science and Technology* **29**,
401 155 (2010).
- 402 6. Chadwick, R. A. *et al.* Geological reservoir characterization of a CO₂ storage site: The Utsira Sand,
403 Sleipner, northern North Sea. *Energy* **29**, 1371–1381 (2004).
- 404 7. Fawad, M., Hansen, J. A. & Mondol, N. H. Seismic-fluid detection-a review. *Earth-Science Reviews*
405 103347 (2020).
- 406 8. Simm, R., Bacon, M. & Bacon, M. *Seismic Amplitude: An interpreter's handbook*. (Cambridge
407 University Press, 2014).
- 408 9. Ostrander, Wj. Plane-wave reflection coefficients for gas sands at nonnormal angles of incidence.
409 *Geophysics* **49**, 1637–1648 (1984).
- 410 10. Shuey, R. T. A simplification of the Zoeppritz equations. *Geophysics* **50**, 609–614 (1985).
- 411 11. Rutherford, S. R. & Williams, R. H. Amplitude-versus-offset variations in gas sands. *Geophysics* **54**,
412 680–688 (1989).
- 413 12. Verm, R. & Hiltermann, F. Lithology color-coded seismic sections: The calibration of AVO
414 crossplotting to rock properties. *The Leading Edge* **14**, 847–853 (1995).
- 415 13. Castagna, J. P. & Swan, H. W. Principles of AVO crossplotting. *The leading edge* **16**, 337–344
416 (1997).
- 417 14. Goodway, B., Chen, T. & Downton, J. Improved AVO fluid detection and lithology discrimination
418 using Lamé petrophysical parameters; “ $\lambda\rho$ ”, “ $\mu\rho$ ”, & “ λ/μ fluid stack”, from P and S inversions. in
419 *SEG Technical Program Expanded Abstracts 1997* 183–186 (Society of Exploration Geophysicists,
420 1997).
- 421 15. Whitcombe, D. N., Connolly, P. A., Reagan, R. L. & Redshaw, T. C. Extended elastic impedance for
422 fluid and lithology prediction. *Geophysics* **67**, 63–67 (2002).

- 423 16. Avseth, P., Veggeland, T. & Horn, F. Seismic screening for hydrocarbon prospects using rock-
424 physics attributes. *The Leading Edge* **33**, 266–274 (2014).
- 425 17. Avseth, P. & Veggeland, T. Seismic screening of rock stiffness and fluid softening using rock-
426 physics attributes. *Interpretation* **3**, SAE85–SAE93 (2015).
- 427 18. Avseth, P., Mukerji, T. & Mavko, G. *Quantitative seismic interpretation: Applying rock physics*
428 *tools to reduce interpretation risk*. (Cambridge university press, 2005).
- 429 19. Avseth, P., Mukerji, T., Mavko, G. & Dvorkin, J. Rock-physics diagnostics of depositional texture,
430 diagenetic alterations, and reservoir heterogeneity in high-porosity siliciclastic sediments and
431 rocks—A review of selected models and suggested work flows. *Geophysics* **75**, 75A31-75A47
432 (2010).
- 433 20. Ødegaard, E. & Avseth, P. A. Well log and seismic data analysis using rock physics templates. *First*
434 *break* **22**, (2004).
- 435 21. Alvarez, P., Bolívar, F., Di Luca, M. & Salinas, T. Multiattribute rotation scheme: A tool for
436 reservoir property prediction from seismic inversion attributes. *Interpretation* **3**, SAE9–SAE18
437 (2015).
- 438 22. Johansen, T. A., Jensen, E. H., Mavko, G. & Dvorkin, J. Inverse rock physics modeling for reservoir
439 quality prediction. *Geophysics* **78**, M1–M18 (2013).
- 440 23. Bredesen, K., Jensen, E. H., Johansen, T. A. & Avseth, P. Seismic reservoir and source-rock analysis
441 using inverse rock-physics modeling: A Norwegian Sea demonstration. *The Leading Edge* **34**,
442 1350–1355 (2015).
- 443 24. Landrø, M. Discrimination between pressure and fluid saturation changes from time-lapse seismic
444 data. *Geophysics* **66**, 836–844 (2001).
- 445 25. Berryman, J. G. *Discrimination of porosity and fluid saturation using seismic velocity analysis*.
446 (Google Patents, 2001).
- 447 26. Behzadi, H., Alvarado, V. & Mallick, S. CO₂ saturation, distribution and seismic response in two-
448 dimensional permeability model. *Environmental science & technology* **45**, 9435–9441 (2011).

- 449 27. Johnson, C. E. Prediction of oil recovery by waterflood—a simplified graphical treatment of the
450 dykstra-parsons method. *Journal of Petroleum Technology* **8**, 55–56 (1956).
- 451 28. Wang, Z., Harbert, W. P., Dilmore, R. M. & Huang, L. Modeling of time-lapse seismic monitoring
452 using CO₂ leakage simulations for a model CO₂ storage site with realistic geology: Application in
453 assessment of early leak-detection capabilities. *International Journal of Greenhouse Gas Control*
454 **76**, 39–52 (2018).
- 455 29. Gassmann, F. Über die elastizität poröser medien: Vierteljahrsschrift der Naturforschenden
456 Gesellschaft in Zurich 96, 1-23. *Paper translation at <http://sepwww.stanford.edu/sep/berryman/PS/gassmann.pdf>* (1951).
- 457
- 458 30. Souza, R., Lumley, D. & Shragge, J. Estimation of reservoir fluid saturation from 4D seismic data:
459 effects of noise on seismic amplitude and impedance attributes. *Journal of Geophysics and*
460 *Engineering* **14**, 51–68 (2017).
- 461 31. Delas, G., Beauchomp, J. B., de Lombares, G., Fourmann, J. M. & Postic, A. An example of practical
462 velocity determinations from seismic traces. in *32nd EAGE meeting in Edinburgh, Scotland* (1970).
- 463 32. Lindseth, R. O. Approximation of acoustic logs from seismic traces: *J. Canadian Well Logging*
464 *Society* **5**, 13–26 (1972).
- 465 33. Fatti, J. L., Smith, G. C., Vail, P. J., Strauss, P. J. & Levitt, P. R. Detection of gas in sandstone
466 reservoirs using AVO analysis: A 3-D seismic case history using the Geostack technique. *Geophysics*
467 **59**, 1362–1376 (1994).
- 468 34. Ma, X.-Q. Simultaneous inversion of prestack seismic data for rock properties using simulated
469 annealing. *Geophysics* **67**, 1877–1885 (2002).
- 470 35. Mindlin, R. D. Compliance of elastic bodies in contact. *J. Appl. Mech., ASME* **16**, 259–268 (1949).
- 471 36. Hashin, Z. & Shtrikman, S. A variational approach to the theory of the elastic behaviour of
472 multiphase materials. *Journal of the Mechanics and Physics of Solids* **11**, 127–140 (1963).
- 473 37. Backus, G. E. Long-wave elastic anisotropy produced by horizontal layering. *Journal of*
474 *Geophysical Research* **67**, 4427–4440 (1962).

- 475 38. Fawad, M., Rahman, M. J. & Mondol, N. H. Seismic reservoir characterization of potential CO₂
476 storage reservoir sandstones in Smeaheia area, Northern North Sea. *Journal of Petroleum Science*
477 *and Engineering* 108812 (2021).
- 478 39. Fawad, M. & Mondol, N. H. Monitoring geological storage of CO₂: a new approach. *Scientific*
479 *Reports* **11**, 1–9 (2021).
- 480 40. Park, J., Bjørke, A. K., Sauvin, G., Morten, J. P. & Nazarian, B. Marine CSEM for CO₂ Storage
481 Monitoring-North Sea Sensitivity Study. in *81st EAGE Conference and Exhibition 2019* vol. 2019 1–
482 5 (European Association of Geoscientists & Engineers, 2019).
- 483 41. (OED) Norwegian Ministry of Petroleum and Energy. *Feasibility study for full-scale CCS in Norway*,
484 *OED report 15/1785, Document A Smeaheia*. (2016).
- 485 42. Fawad, M., Rahman, M. J. & Mondol, N. H. Seismic-derived geomechanical properties of potential
486 CO₂ storage reservoir and cap rock in Smeaheia area, northern North Sea. *The Leading Edge* **40**,
487 254–260 (2021).
- 488 43. NPD. Norwegian Petroleum Directorate Fact-pages. <https://factpages.npd.no/> (2021).
- 489 44. Kinn, S. *et al. Final Well Report 32/4-1*. <https://factpages.npd.no/en/wellbore> (1997).
- 490 45. Avseth, P., Janke, A. & Horn, F. AVO inversion in exploration—Key learnings from a Norwegian
491 Sea prospect. *The Leading Edge* **35**, 405–414 (2016).
- 492 46. Wyllie, M. R. J., Gregory, A. R. & Gardner, L. W. Elastic wave velocities in heterogeneous and
493 porous media. *Geophysics* **21**, 41–70 (1956).
- 494 47. Lee, M. W. *Velocity ratio and its application to predicting velocities*. (US Department of the
495 Interior, US Geological Survey, 2003).
- 496 48. Mavko, G., Mukerji, T. & Dvorkin, J. *The rock physics handbook: Tools for seismic analysis of*
497 *porous media*. (Cambridge University Press, 2009).
- 498 49. Archie, G. E. The electrical resistivity log as an aid in determining some reservoir characteristics.
499 *Transactions of the AIME* **146**, 54–62 (1942).

- 500 50. Reuss, A. Berechnung der Fleissgrenze von Mischkristallen auf Grund der Plastizitäts bedingung
501 für Einkristalle. *Zeitschrift für Angewandte Mathematics aus Mechanik* **9**, 49–58 (1929).
- 502 51. Brie, A., Pampuri, F., Marsala, A. F. & Meazza, O. Shear sonic interpretation in gas-bearing sands.
503 in *SPE Annual Technical Conference and Exhibition* (Society of Petroleum Engineers, 1995).
- 504 52. Castagna, J. P., Batzle, M. L. & Eastwood, R. L. Relationships between compressional-wave and
505 shear-wave velocities in clastic silicate rocks. *Geophysics* **50**, 571–581 (1985).

506

507 **Acknowledgments**

508 The authors thank the University of Oslo for providing the material, financial support, and facilitation
509 to publish this paper under the OASIS (Overburden Analysis and Seal Integrity Study for CO₂
510 Sequestration in the North Sea), NFR-CLIMIT project #280472. We are grateful for the financial
511 support provided by the Research Council of Norway, Equinor and Total for the OASIS project and
512 Eni Norge (now Vår Energi AS) for funding the "ReSource – Quantitative analysis of reservoir, cap,
513 and source rocks of the Central North Sea" R&D project. Schlumberger has provided academic
514 software licenses for PETREL and dGB Earth Sciences for OPENDTECT.

515

516 **Competing interests**

517

518 M.F. and N.H.M. applied for a grant of a patent (Application number 20210087 & US63/140,891) of
519 the "Rock physics model for fluid identification and saturation estimation in subsurface reservoirs"
520 procedure as inventors and owners. The status is "Patent Pending." The Methods section is covered in
521 the patent application.